of complexation of the counterion. This extra stabilization from the counterion and the shielding effects give us a possible explanation of the difference between the gas-phase result and the solution result.

Our original hypothesis of a charge relay from the C_3 carbanionic bridge to the C_2 olefinic bridge in anion I via lithium p orbitals has not found support in these calculations. True, the lithium cation was found to occupy the proposed position between the π systems of the two bridges, but its interaction is mostly electrostatic in nature. The rehybridization of C_6 and C_7, the coordination of these carbons with the lithium cation, and a considerable redistribution of charge through bonds might be responsible for the unusual NMR spectral properties of I.[4]

Conclusion

The results obtained in the present study do not give any indication that bishomoaromaticity is an important factor in the chemistry of anion I and related carbanions. Rather, it seems possible to explain the 30-year-old controversy[1] in terms of the quadrupolar property of the C_2 olefinic bridge in anion I and the role of the counterion in solution. Such explanations have not been considered in earlier work.

It may be argued that this study is too primitive to allow firm conclusions to be drawn. Notably, the basis sets used in the calculations are rather limited, and it has only been possible to account for the most important part of the correlation effects, the near degeneracy correlation in the π system of the carbanion. Even if calculations using larger basis sets (especially including diffuse 2p-type functions on the carbon atoms in the allylic bridge) would be of value, we do not believe that the results would be very different from those obtained in the present study. The net interaction between the allylic and the olefinic part of the ion would still be repulsive rather than attractive.

Acknowledgment. We acknowledge helpful discussions with Prof. P. v. R. Schleyer and docent Gunnar Karlström. We are also grateful to E. Kaufmann, R. R. Squires, F. H. Köhler, and P. v. R. Schleyer for providing us with their manuscripts prior to publication. This project was supported by a grant from the Swedish Natural Science Research Council (NFR).

Registry No. C_2H_4, 74-85-1; C_3H_5, 1981-80-2; $C_3H_5^-$, 1724-46-5; LiC_3H_5, 3052-45-7; $C_8H_9^-$, 76881-29-3; LiC_8H_9, 101671-14-1.

Electronic Structure of Transition-Metal Borides with the AlB_2 Structure

Jeremy K. Burdett,* Enric Canadell,† and Gordon J. Miller

Contribution from the Department of Chemistry, The University of Chicago, Chicago, Illinois 60637. *Received April 9, 1986*

Abstract: A study of the electronic structure of solid metal borides with the AlB_2 structure type is presented. The interaction of the orbitals of the transition metal with those of a planar, graphite-like net of boron atoms and the interaction with those of other metals are both important in influencing the properties of these species. It is suggested that the experimentally observed variation in the heat of formation of these species is crucially dependent upon the extent of occupation of the metal–boron orbital set. In addition it appears that the puckering of the boron net in ReB_2 and RuB_2 structures is due not to the obvious effects of charge transfer but to strong metal–metal repulsions perpendicular to the nonmetal sheets. In AlB_2 itself the strongest interactions are between the boron atoms which attain a graphite-like electron count with its associated structural stability.

The AlB_2 structure[1] is one which is adopted by many of the transition-metal diborides (Table I). It may be regarded (Figure 1) as a completely intercalated graphite in the sense that all of the hexagonal prismatic sites of the primitive graphite structure are filled. The empty primitive lattice is unknown for carbon itself but is found for the derivative BN. (In carbon adjacent sheets are displaced with respect to each other.) Derivative AlB_2 systems are also known. NaBeAs is an example, where the 6^3 nets contain alternatively Be and As. In several of the examples with this structure, such as MgB_2, $CaGa_2$, and NaBeAs, if electron transfer from the intercalated atom to the sheet is assumed to be complete, then the sheet itself is isoelectronic with graphite or a heavier group 14 analogue (B^-, Ga^-, $BeAs^-$). Addition of electrons leads to a nonplanar sheet. $CaSi_2$, for example (Figure 2), contains puckered silicon sheets, just like those found in the structures of elemental As, Sb, and Bi. Si^- is, of course, isoelectronic with the group 15 elements. Transition-metal diborides with the AlB_2 structure are known for the first-row elements Sc through Mn. Obviously here there is not complete electron transfer from the metal to the boron sheet. For the second- and third-row transition-metal series a changeover in structure occurs between groups 6 and 7 and between 7 and 8. The RuB_2 structure is one composed of puckered graphite sheets and is related[2] to the structure of "tetragonal carbon". The mode of puckering is different to that found in $CaSi_2$, and the result is perhaps best described as the generation of corrugated sheets. The structure of ReB_2 and TcB_2 (*hP*6) is very similar to that of $CaSi_2$ (*hR*6) and only differs in the way the puckered sheets are stacked. **1** and **2** show the metal coordination geometry in the structures of AlB_2 and ReB_2. In the former the metal is 12 coordinate and in the latter 8 coordinate. In this paper we examine the interaction of the metal with the

Table I. Occurrence of Borides with the AlB_2 or Related Structures

Mg								
X								
Ca	Sc	Ti	V	Cr	Mn	Fe	Co	Ni
	X	X	X	X	X			
Sr	Y	Zr	Nb	Mo	Tc	Ru	Rh	Pd
		X	X	X	X[a]	X[b]		
Ba	La	Hf	Ta	W	Re	Os	Ir	Pt
		X	X		X[a]	X[b]		

[a] Puckered sheet. [b] Corrugated sheet.

† Present address: Laboratoire de Chimie Theorique, Universite de Paris-Sud, Orsay 91405, France.

(1) See, for example: (a) Pearson, W. B. *Crystal Chemistry and Physics of Metals and Alloys*; Wiley: New York, 1972. (b) Aronsson, B.; Lundstrom, T.; Rundqvist, S. *Borides, Silicides and Phosphides*; Wiley: New York, 1965. (c) *Boron and Refractory Borides*; Matkovich, V. I., Ed.; Springer-Verlag: New York, 1977.

(2) Burdett, J. K.; Canadell, E., unpublished results.

0002-7863/86/1508-6561$01.50/0

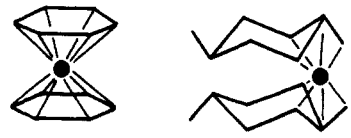

1 2

boron sheets in these systems and show how it controls their structure.

Electronic Structure of MB_2 Species with the AlB_2 Geometry

Figure 3 shows the electronic density of states for an MB_2 species (M = transition metal) in the AlB_2 structure as calculated via a band-structure calculation[3,4] of the extended Hückel type, with parameters given in the Appendix. The results we will present are in qualitative terms broadly independent of the nature of the metal. Quantitative differences are found however, and sometimes we will report the results of two sets of calculations, one with parameters appropriate for Ti (an early transition metal) and one with parameters appropriate for Fe (a late transition metal). A prominent feature of the plot of Figure 3 is the presence of two peaks in the region of interest. One is located at the Fermi level appropriate for a metal close to Ca and the other for a metal between Mn and Fe. Also shown is the decomposition of the total density of states into contributions from the three types of d orbitals suggested by the local symmetry **1**, namely, z^2, (xy, x^2-y^2), and (xz,yz). In the region containing the Fermi levels of MB_2 species for the first-row transition-metal series the orbitals contain large amounts of d orbital character. Notice that the two peaks in the total density of states are dominated by contributions from z^2.

One of the interesting features of the interaction of metal and boron is associated with the relative energies of the atomic orbitals concerned. Since the metal 3d levels lie between the boron valence 2s and 2p orbitals, the energies of the metal levels lie in a region of the energy band where the boron–boron interactions are bonding ones. Figure 4 shows COOP (crystal orbital overlap population) curves for the linkages of these systems. The B–B overlap population never becomes negative in the region of chemical interest. As a result, the increase in the number of electrons with metal d count leads to a strengthening of these bonds, and the B–B distance should shorten across the series. A double plot which shows the overlap population and bond length variations appears in Figure 5. The general trend expected on the basis of these simple theoretical ideas is found experimentally. Table II gives values of the geometric parameters.

Important interactions in these species occur between metal and boron orbitals. An analysis of the orbitals of the MB_{12} fragment **3** gives results which are similar to those for the in-

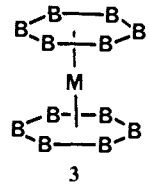

3

teraction of metal and benzene orbitals in the molecular species dibenzenechromium, for example, which has been discussed elsewhere.[5] We shall focus here on the behavior of the z^2 orbital. Figure 6 shows the behavior of the relevant orbitals on assembly of the fragment **3**. Since the ring lies close to a conical node of z^2 (**4**) with $\theta = 54.73°$, the interaction of this orbital with the orbitals of the ring is not large, and small energy shifts result.

(3) There are earlier band-structure calculations on these systems: (a) Armstrong, D. R. *Theor. Chim. Acta* **1983**, *64*, 137. (b) Ihara, H.; Hirabayashi, M.; Nakagawa, H. *Phys. Rev. B: Solid State* **1977**, *B16*, 726. (c) Liv, S. H.; Kopp, L.; England, W. B.; Myron, H. W. *Phys. Rev. B: Solid State* **1975**, *B11*, 3463.

(4) For links between the orbital structures of solids and molecules, see: (a) Burdett, J. K. *Prog. Solid State Chem.* **1984**, *15*, 173. (b) Hoffmann, R.; Wijeyesekera, S. D.; Sung, S. *Pure Appl. Chem.*, in press.

(5) (a) Burdett, J. K.; Canadell, E. *Organometallics* **1985**, *4*, 805. (b) Lauher, J.; Elian, M.; Summerville, R.; Hoffmann, R. *J. Am. Chem. Soc.* **1976**, *98*, 3219.

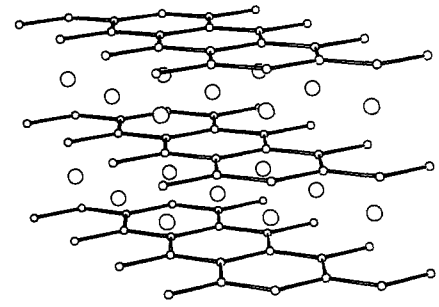

Figure 1. Structure of AlB_2.

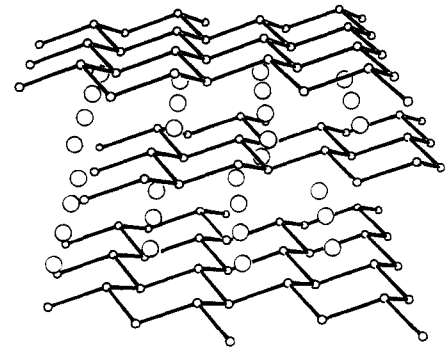

Figure 2. Structure of $CaSi_2$.

Table II. Geometrical Data for Transition-Metal Diborides with the AlB_2 Structure

metal	M–B, Å	B–B, Å	$M-M_\perp$, Å
Sc	2.53	1.816	3.517
Ti	2.38	1.748	3.228
V	2.30	1.727	3.050
Cr	2.30	1.714	3.066
Mn	2.31	1.736	3.037

Notice how the pure π orbitals of the ring have tilted over as a consequence of admixture of some in-plane σ contribution. A bonding, approximately nonbonding, and antibonding trio of orbitals results. In the extended array such a simple picture is broadened into bands by through-bond coupling and shifted energetically too by metal–metal interactions. The width of the bands is determined by the sizes of the interaction between metal and boron and by the size of direct metal–metal interactions both through the B_6 ring and within the sheets. For the z^2 orbital the dominant metal–metal interaction occurs perpendicular to the sheets, where the large lobes are directed. Much smaller overlap (approximately one-quarter as large) is found for interactions parallel to the sheets. Since, as we have just described, the node of z^2 lies in an orientation (**4**) so that the interaction with the boron

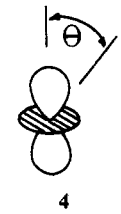

4

orbitals of the ring is relatively small, the width of the z^2 bands is smaller than those associated with the other d orbitals where such a restriction does not occur. This is clear to see in Figure 3. The concentration of z^2 character into these two regions as a result has important implications, as we will see later.

Figure 7 shows the dispersion of the energy bands along the line Δ of the hexagonal zone **5**. This is the direction in reciprocal space where energetically interesting and important interactions occur. These are the interactions with the boron ring orbitals and the "through-ring" metal–metal interaction. At Γ, orbitals of even parity on the metal may not mix with the in-phase com-

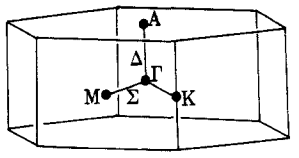

5

bination of boron pπ orbitals. As a result the higher energy crystal orbital labeled a_1 is simply the boron ring orbital stabilized by some admixture of metal p_z. At A this orbital has now become the out-of-phase combination along z of a metal-centered s–d hybrid. The sense of the hybridization is such that the hybrid is well directed along z. The amount of z^2 character increases on moving along the Δ line in k space, reaching a maximum at the point A. (Compare the energy of the crystal orbital at this point in Figure 7 with the energy at the maximum in the z^2 projection of Figure 3.) At this point too, because of the enforced phase relationships from cell to cell in this direction, this crystal orbital is antibonding between the metal atoms perpendicular to the sheets. Its energy is then controlled by these direct metal–metal interactions. The lower energy z^2 band of Figure 3 is, from Figure 7, purely metal located at Γ. The enforced cell-to-cell phase relationships at this point mean that the orbital is bonding between the metal atoms along z. The z^2 character in this orbital decreases on moving along the line Δ. Figure 8 shows the dispersion along the line Σ of the zone. The orbital indicated with arrows is largely composed of z^2 at Γ (as seen in Figure 7). It mixes strongly on moving along the line Σ with one component of what was a doubly degenerate band at Γ built from an admixture of x^2-y^2 and xy orbitals. The result is clear to see: the z^2 contribution occurs over a rather narrow energy range. The rather sharp features associated with the z^2 projection of Figure 3 are then quite understandable.

The interplay of the effects of metal–metal and metal–boron interaction for the orbital problem as a whole is shown in the set of COOP curves of Figure 5 for the B–B, M–B, and the two types of M–M interactions, parallel and perpendicular to the planes of boron atoms. Notice that (using Ti parameters) antibonding M–M orbitals begin to be populated just after M = Ti and antibonding M–B orbitals just after M = V. We will describe some of the consequences of these results in the sections below.

Heat of Formation

Figure 9a shows the variation in the heats of formation of the first-row diborides as recently determined experimentally by Kleppa and Topor.[6] A prominent feature is the maximum at M = Ti. This corresponds to 10 electrons per unit cell, i.e., per MB_2 unit. Figure 9b shows our calculated variation in the stabilization energy of crystalline TiB_2 as the d count increases. (The quantity plotted is the computed stabilization energy of a d^n system minus the energy of the relevant number of free metal d electrons.) Quantitatively the agreement is poor; problems are associated with both the rigid band approximation and the nature of our one-electron calculation, but the broad qualitative similarity between the two plots is striking. An examination of the plots for some other systems will lead to an understanding of the shape of the heat of formation curve. Our approach will focus purely on electronic effects. While geometric effects[7] may well be important, we are not able to rigorously separate the two. A computation for FeB_2, using the same geometrical details as before but with orbital parameters appropriate for iron rather than for titanium, also leads to a peaked curve (shown in Figure 9c) but with a maximum now at the d count for M = Sc (nine electrons per unit cell) rather than at M = Ti. A similar computation for the hypothetical MC_2 system shows a maximum (Figure 9d) at M = Ni (18 electrons per unit cell).

6 shows a simple model which may be used to understand these results. Consider a set of metal d levels which will "dissolve" into a sea of nonmetal (X) orbitals located in a band of given width. If the dominant interactions are between the nonmetal atoms, then

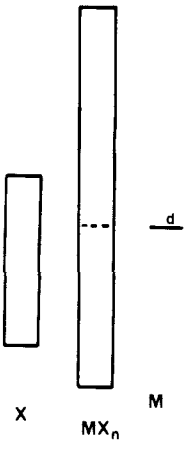

6

the orbitals which contain M–X bonding character will lie below the dashed line and those with M–X antibonding character above the line. As the M–X interactions become stronger, this statement becomes less rigorous, but the qualitative result is similar. For a given d count the available electrons will first fill M–X bonding orbitals and then, as the electron count increases, eventually M–X antibonding orbitals. Filling bonding orbitals leads to a positive slope in the curves of Figure 9, and filling antibonding orbitals leads to a negative slope. This is an argument exactly analogous to that used[8] to understand the variation with d count of the cohesive energies of the solid transition metals, the elements of the sp block, and indeed the bond lengths, force constants, and dissociation energies of diatomic molecules such as N_2 and F_2. As the energy separation between the metal d levels and the centroid of the nonmetal levels increases, then more electrons per formula unit will be required to start to fill these antibonding levels. For TiC_2 with a large gap between metal d and nonmetal s,p orbitals (7), Ti–C antibonding levels are not filled until the electron

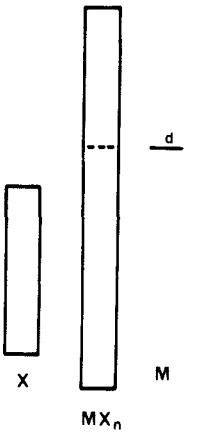

7

count corresponds to NiC_2, but for the borides where the metal d levels lie between the nonmetal atomic 2s and 2p levels, the M–B bonding levels are filled early in the transition-metal series, and a prominent feature of the curve is its negative slope past Sc or Ti. Unfortunately, metal dicarbides of this type are not known, and so we cannot test out this result. Notice that the shift in the maximum in the plots for MB_2 on moving from M = Ti to M = Fe, by increasing the d orbital ionization potential, is in accord with such an approach. In principle then it should be a simple matter to predict the qualitative features at least of curves of the type shown in Figure 9 for many metal/nonmetal systems, by a simple examination of the metal and nonmetal ionization energies. The picture may well be more complex, however, for metal-rich borides where metal–metal bonding is extensive.

(6) Topor, L.; Kleppa, O. *J. Chem. Thermodyn.* **1985**, *17*, 1003.
(7) Spear, K. E. *J. Less-Common Met.* **1976**, *47*, 195.
(8) Albright, T. A.; Burdett, J. K.; Whangbo, M.-H. *Orbital Interactions in Chemistry*; Wiley: New York, 1985.

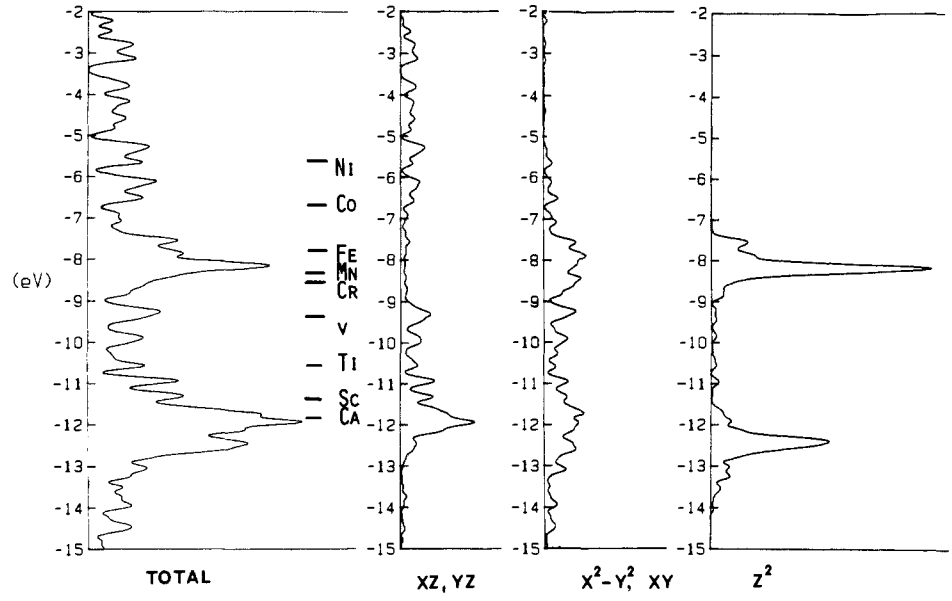

Figure 3. Electronic density of states for MB_2 species in AlB_2 structure. M = transition metal. Also shown is the decomposition of the total density of states into contributions from z^2, (x^2-y^2,xy), and (xy,yz). The Fermi levels corresponding to various first-row metals in the rigid band approximation are shown. (The results shown are from a calculation of TiB_2.) The z^2 contribution in the right-hand panel has been multiplied by a factor of 2.

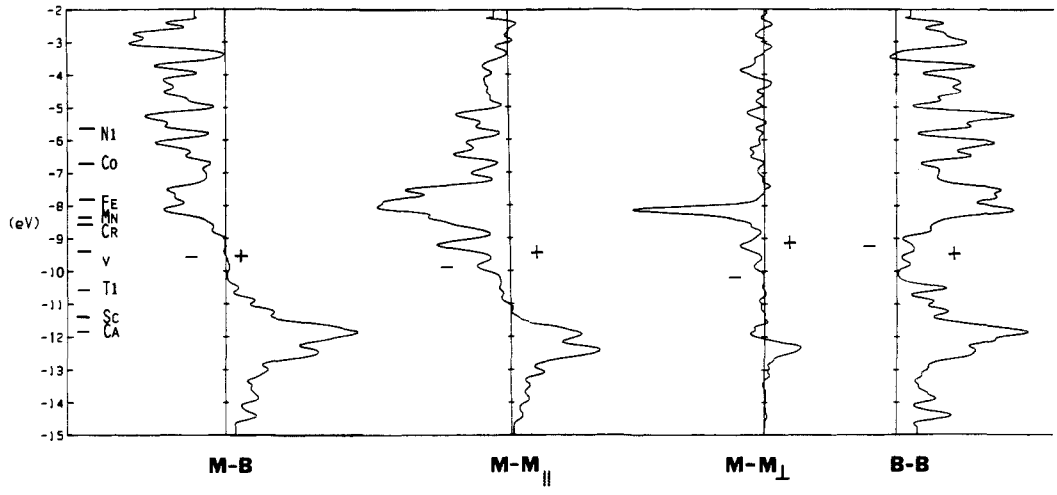

Figure 4. Crystal orbital overlap population curves (COOP curves) for the four different types of interactions in the AlB_2 structure.

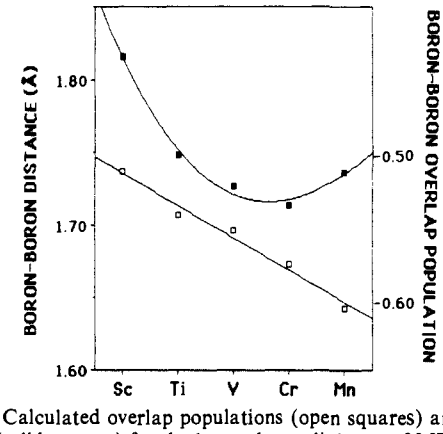

Figure 5. Calculated overlap populations (open squares) and observed distances (solid squares) for the boron–boron linkages of MB_2 species as a function of d count. (Geometrical data from the compendium in ref 6.)

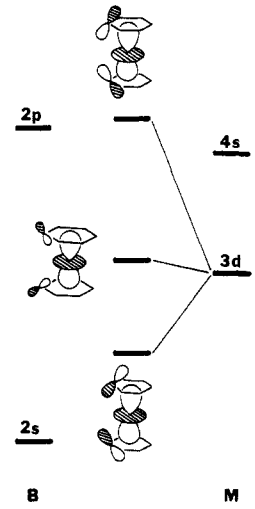

Figure 6. Interaction of the metal z^2 and s orbitals with the relevant boron orbitals in the MB_{12} fragment. For the sake of simplicity all other interactions are not shown. The diagram is a qualitative one.

Our model also allows us to see how the maximum in the curve moves as a function of the stoichiometry. Elsewhere,[2] for MB_4 systems based on the tetragonal carbon net we have described how for MB_4 systems the maximum occurs at M = Cr, and it is easy to qualitatively understand this computed result. The number of metal levels introduced into the sea of boron orbitals depends upon x if the formula is written as BM_x. The number of M–B

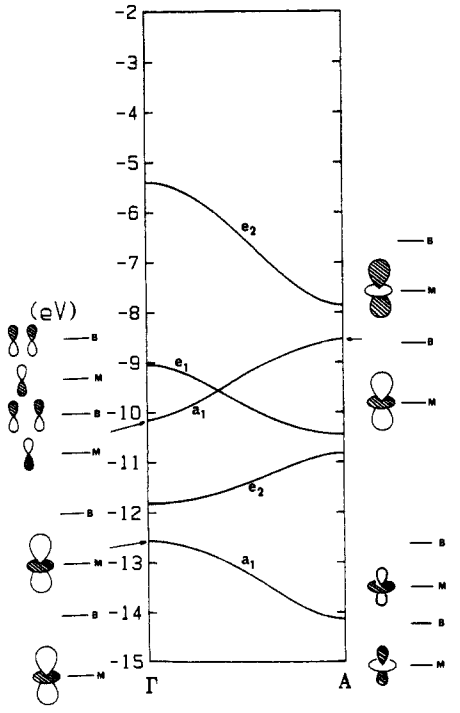

Figure 7. Dispersion of some of the energy bands of MB_2 systems along the line Δ of the hexagonal zone.

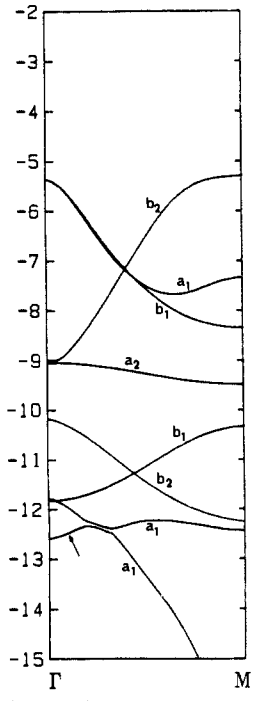

Figure 8. Dispersion of some of the energy bands of MB_2 systems along the line Γ of the hexagonal zone.

bonding orbitals depends directly on x too. It then takes fewer electrons to fill all the M–B bonding orbitals for MB_4 ($x = 0.25$) than for MB_2 ($x = 0.5$). Indeed the maxima are found for Cr in MB_4 (1.5 electrons per metal per boron) and Ti in MB_2 (2.0 electrons per metal per boron). The quantitative prediction of the location of the maximum, and how it moves, for example, on going from MB_2 to MB_4, is much more difficult. Sometimes the change in the shape of the plot relative to the elements of the transition-metal series has a simple explanation. For example, our computations on MSi_2 species in the $TiSi_2$ structure show (Figure 9e) a heat of formation plot which decreases from M = Sc without peaking in the series. Silicon and boron have similar valence ionization potentials, as expected via the diagonal relationship, but such a result is simply understandable given that the

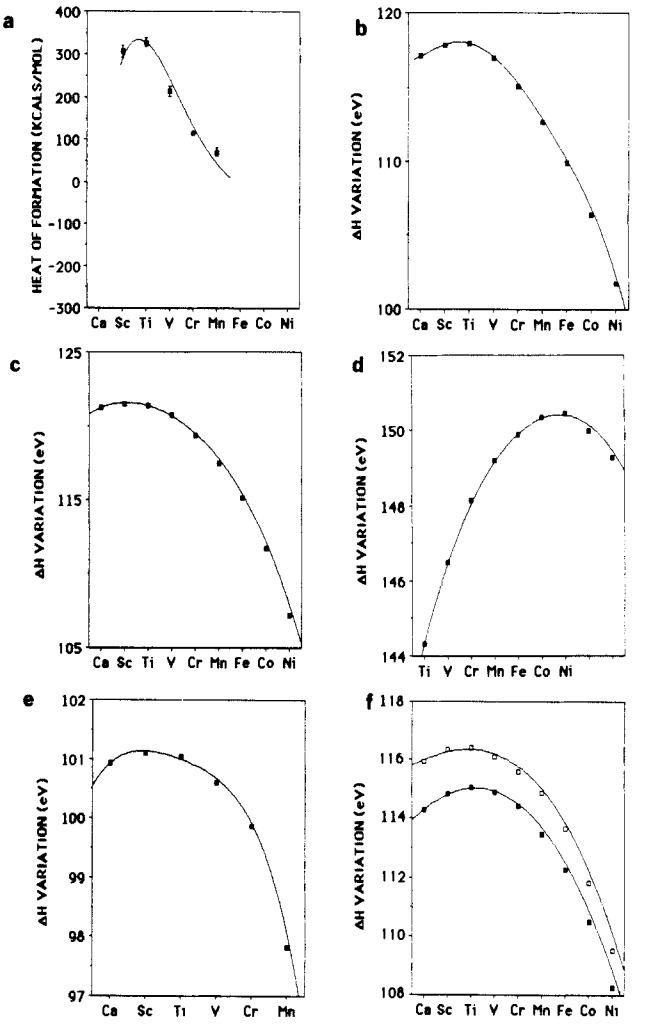

Figure 9. Variations in the heats of formation of metal borides and silicides. (a) Experimental values for the heats of formation for the first-row diborides from ref 6. (b) Calculated variation in the heat of formation of the diborides as a function of d count using the results of a computation on TiB_2 in the AlB_2 structure. (c) Same as b, but using a calculation on FeB_2. (d) Same as b, but using TiC_2. (e) Calculated variation in the heat of formation of the first-row disilicides as a function of d count using the results of a computation on $TiSi_2$ with the geometry of the $TiSi_2$ structure. (f) Calculated variation in the heat of formation of the first-row diborides in the fluorite (open squares) and cadmium iodide (closed squares) structures from computations on TiB_2.

maximum still occurs at close to 10 electrons per formula unit, silicon contributing 4 electrons compared to boron's 3. The computed result is in qualitative agreement with experimental results[9] on those systems which crystallize in the $TiSi_2$ or a related structure type, which show a decreasing heat of formation from M = Ti to M = Cr. An estimate[9] for the heat of formation for the unknown $ScSi_2$ puts it higher than that for $TiSi_2$.

That the shape of these plots is broadly independent of structure is shown by consideration of the curves of Figure 9f. They depict the corresponding variations in stabilization energy for MB_2 systems in the fluorite and cadmium iodide arrangements and have the same general shape as the curve for the AlB_2 geometry. It is dangerous to rely on computed one-electron energy differences between these structures with such very different coordination numbers, but it is interesting to note that MSi_2 species are found in the fluorite arrangement at the right-hand side of the series (for M = Co and Ni). The heats of formation of MSi_2 species (M = Mn through Ni) gently rise[9] on moving from left to right across the series, a result at variance with our overall scheme. We

(9) Kleppa, O.; Topor, L., unpublished results on silicides.
(10) Whangbo, M.-H.; Hoffman, R.; Woodward, R. B. *Proc. R. Soc. London, A* **1979**, *A366*, 23.

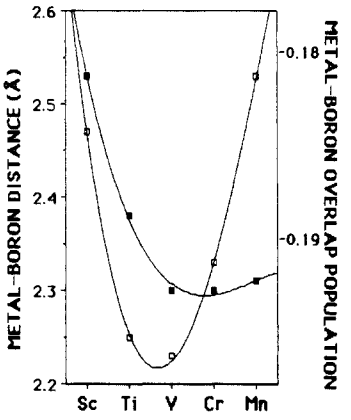

Figure 10. Computed bond overlap populations (open squares) and observed distances (solid squares) for the metal–boron linkages of MB_2 species as a function of d count. (Geometrical data from the compendium in ref 6.)

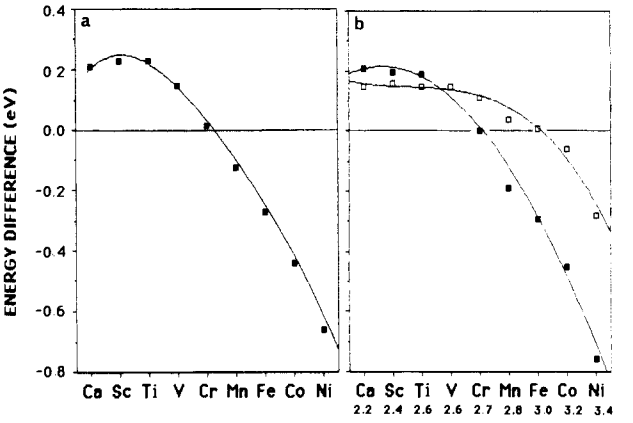

Figure 11. Energy difference curves as a function of d count for planar and puckered AlB_2 geometries. (a) Results from calculations on TiB_2 in the AlB_2 and ReB_2 structures. (b) Results from calculations on TiB_2 (solid squares) and FeB_2 (open squares) in the AlB_2 and puckered AlB_2 geometries. In b we show the boron atom charges as a function of electron count for TiB_2.

are unable at this stage to tell whether this is due to changes in crystal structure at this point or to the naiveté of our model.

This approach may be quite a useful one to look at, in general, the qualitative form of the phase diagram associated with a metal/nonmetal system. The variation in the heat of formation of species with different stoichiometry will form a series of parabolic curves centered at different electron counts. The energy difference between two phases of different stoichiometry will then be a sensitive function of electron count too. We have described[2] how size effects are also important in controlling the stability of these borides. VB_4 with the CrB_4 structure is unknown, probably because the vanadium atom is too large to fit into the available holes in the boron net. The more open UB_4 structure type is found for these earlier, and larger, metals.

The form of the metal–boron overlap population curve should be reflected in the actual distances in these borides. A double plot is shown in Figure 10. The actual variation in distance will be controlled by the interplay of the variation in electronic preferences (mirrored by the overlap population) and the change in the radius of the metal. The metal radius decreases on moving to the right of the transition-metal series, and shorter metal–boron distances are to be expected from this source alone. The correlation between the observed distances and the calculated overlap population variation is not at variance with such ideas.

Puckering of the Nonmetal Sheet

Figure 11 shows the energy difference curve we calculate for the AlB_2 structure and structures related to the ReB_2 arrangement as a function of d count. One of the geometries corresponds to a puckered structure where the metal atoms remain in the same positions as in the AlB_2 arrangement but with an increase in the metal–metal separation along the *c* axis. The other corresponds closely to the real ReB_2 structure where the metal coordination site has changed (**1** and **2**) relative to that in AlB_2, leading to a lower metal coordination by boron and a much larger M–M separation along the *c* direction. Notice the crossover in stability relative to AlB_2 along the transition-metal series. (Note also the sensitivity of the plot to the parameter choice.) Our computed result is in broad agreement with the experimental result for the third-row transition-metal series where the crossover has occurred by M = Re (Table I). Also shown on the plot are the nonmetal charges for one of the puckered geometries as a function of electron count. Notice that the sheet puckering occurs at a significantly lower nonmetal density than for the isolated sheets. In $CaGa_2$ where the gallium atoms have close to four electrons, the sheets are planar, but in $CaSi_2$ with a silicon configuration of five valence electrons, the sheets are puckered. In the transition-metal borides the puckering occurs at a computed density of between 2.8 and 3.0 electrons at boron, the number depending on the metal parameters used in the calculation.

This response of the boron net is a little unusual when compared to other chemistry of first- and second-row atoms. Whereas the

Table III. Overlap Populations between the Different Types of M–M Linkages

	⊥	∥
(Ca)	0.04	0.09
Sc	0.04	0.10
Ti	0.04	0.09
V	0.01	0.07
Cr	−0.04	0.03
Mn	−0.14	0.00
(Fe)	−0.16	−0.04
(Co)	−0.17	−0.07

first-row element carbon is known as graphite, and the structure of MgB_2 is that of AlB_2, no such extended array is known for nitrogen. By contrast the second-row and heavier elements of group 15 are well-known as polymers (A7 and A14 structures). The Gedanken experiment of intercalating graphite with calcium to give CaC_2 leads to splitting up of the lattice as shown in eq 1 to give the $C11_a$ structure. This contains isolated C_2^{2-} units, isoelectronic with N_2, rather than the puckered net found in $CaSi_2$. Perhaps the puckering of the nonmetal sheets in the transition-metal borides is then due to effects other than the obvious one of charge transfer.

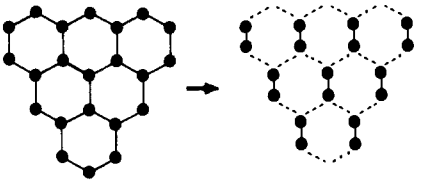

(1)

Such arguments based on the charge distribution are open to objections of course. In $CaSi_2$, where the interaction between metal and nonmetal orbitals is small, the value of five electrons per silicon is a valid number, but in the transition-metal diborides, where the interaction is strong, the meaning of the atomic populations is open to question. The mechanics of dividing up the electron density in the form of atomic populations and overlap populations (which we discuss below) is somewhat arbitrary and by no means foolproof in terms of providing clear-cut answers to questions of this sort. There has been considerable debate over the direction of charge transfer in these borides for some years (see ref 1c, for example). Transfer from boron to metal seems to be the accepted direction, supported by magnetic measurements.[11]

(11) (a) Castaing, J.; Danan, J.; Rieux, M. *Solid State Commun.* **1972**, *10*, 563. (b) Castaing, J.; Caudron, R.; Toupance, G.; Costa, P. *Solid State Commun.* **1969**, *7*, 1453. (c) Cadeville, M. *J. Phys. Chem. Solids* **1966**, *27*, 667.

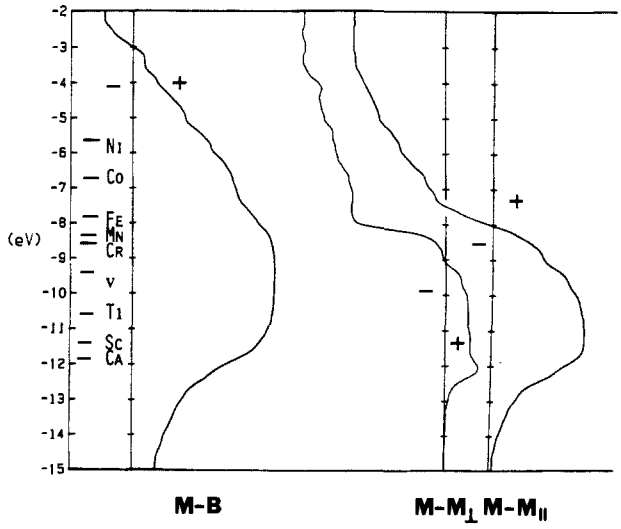

Figure 12. Integrated COOP curves of Figure 5 for the two different M–M and the M–B linkages.

There is another explanation for the puckering of the nonmetal sheets which we find attractive. Table III shows the values for the metal–metal overlap populations both parallel (**8**) and perpendicular (**9**) to the nonmetal sheets as a function of the d electron count or the transition metal in the AlB_2 structure. Integrated

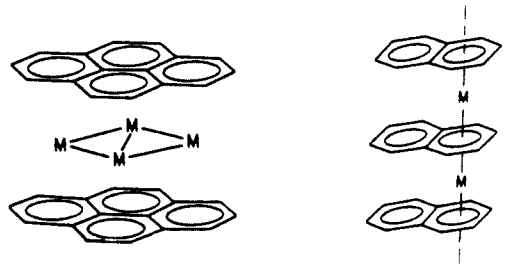

8 **9**

COOP curves for these two interactions are shown in Figure 12. Notice that as the d count increases the perpendicular M–M interactions are associated with a very negative overlap population of the antibonding part of the z^2 band as described earlier. This is much more negative than the population associated with the in-plane interactions. The concentration of z^2 character into this narrow region has a very striking effect. Relief of this strong antibonding interaction may occur by stretching the structure along z and puckering the boron sheets so as to retain close M–B distances and a good M–B overlap or by puckering the sheets and moving the metal atoms into the eight-coordinate sites of **2**. This second distortion gives the ReB_2 structure. The results of our computations on these two systems are shown in Figure 11. A similar increase in metal–metal distance occurs during a distortion to the RuB_2 structure. Here the metal atoms are even further apart. A more detailed analysis of this type of distortion coordinate using our methods is inappropriate (changes in coordination number and both M–M and M–B distances are involved), but identification of the puckering distortion with relief of the fierce axial metal–metal antibonding interaction is an appealing one. A distortion of this type at this electron count is completely consistent with the electronic structure of these systems.

It is interesting to compare these results with similar calculations we have performed on AlB_2 itself. Here the direction of charge transfer is from Al to B, the electron density of boron being computed to be 3.81. The boron sheet is then quite close electronically to being a graphite sheet. Both types of Al–Al interaction are repulsive. Negative overlap populations are computed for both $Al–Al_{\parallel}$ and $Al–Al_{\perp}$ linkages. The most striking difference to the transition-metal case is the weakness of the Al–B interaction (overlap population of 0.14) and the strength of the B–B interactions (overlap population of 0.78). These numbers should be

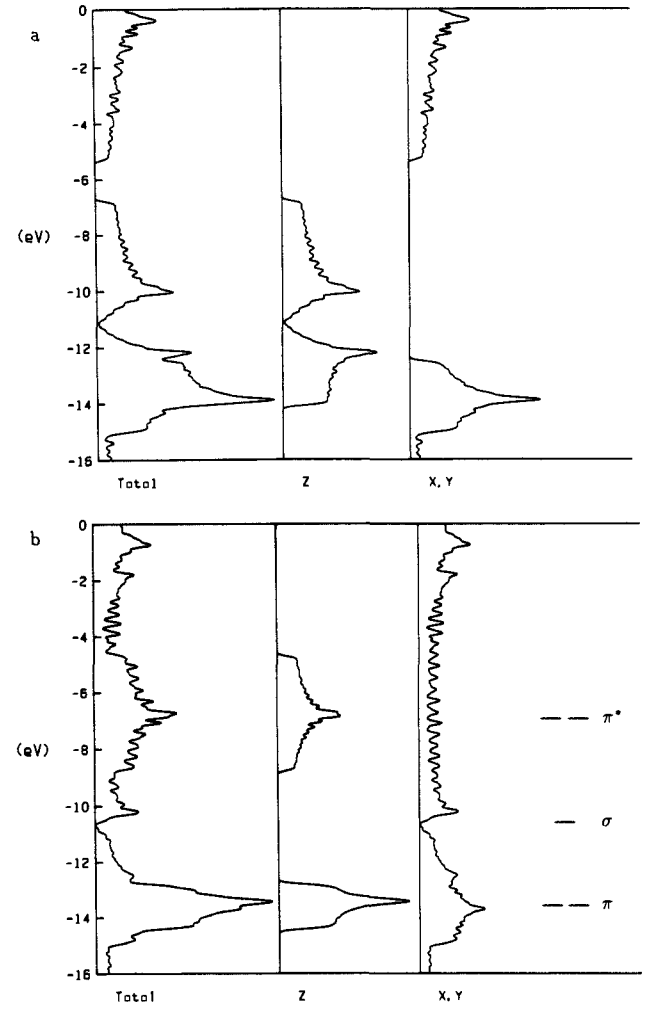

Figure 13. Behavior of the density of states of the graphite net during the distortion of eq. 1. At the top (a) are the densities of states for the graphite net itself (the spiky behavior is due to the use of a finite k point set) and at the bottom (b) those for the brokenup structure. Also shown are the energy levels for an isolated C_2^{2-} unit with the same geometry as that used in b.

compared with those of Figures 10 and 5, respectively. The sheet does not pucker in AlB_2 itself because structurally the system is dominated by strong B–B interactions which at this pseudographite electron count keep it planar.

Breakup of 6^3 Sheets

Figure 13 shows how the energy density of states changes as the graphite net distorts to give a series of "isolated" C_2 dimers as shown in eq 1. This is the (110) nonmetal net of the CaC_2 structure. Though these C_2 dimers (d(C–C) = 1.19 Å) are separated by nearly 2.2 Å, the discrete energy levels of the unit are broadened into bands. The π_z manifold for the electron configuration appropriate for N_2 or C_2^{2-} is full in the graphite geometry but only half-full in the "molecular structure" (see ref 4 and 10 for discussion of the energy bands of the graphite structure). An analysis of the band structure at Γ for various stages of the transformation reveals the orbital crossings anticipated. For the graphite structure the bands are classified according to D_{6h} ($6/mmm$) point symmetry which reduces to D_{2h} ($2/m$) upon distortion and thus splits the p_x, p_y degeneracy. Figure 14 shows that the orbital correlations involve more than simply a σ–π_z symmetry-allowed level crossing. The π_z and π_z* bands, which exactly touch in the graphite structure with a low DOS, become separated as the dimeric network forms. This splitting arises from a stronger π interaction within the dimer and a weaker π interaction between dimers. The σ bands in graphite transform into σ_x and π_y levels in the limit of isolated molecules. The σ_x band remains σ bonding throughout with a component of the σ_{2s} level.

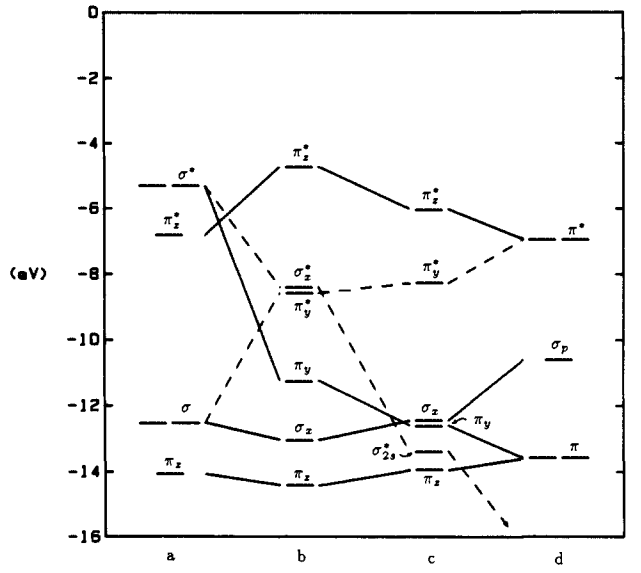

Figure 14. Orbital correlation at Γ from the graphite structure to isolated C_2 dimers via the distorted network shown in eq 1. (a) Graphite geometry; (b) distance between dimers is 2.08 Å; (c) distance between dimers is 2.5 Å; and (d) isolated dimers.

Table IV. Parameters and Exponents Used in the Calculations

atom	orbital	H_{ii}, eV	ζ_1	ζ_2	c_1[a]	c_2
B	2s	−15.20	1.30			
	2p	−8.50	1.30			
C	2s	−21.40	1.625			
	2p	−11.40	1.625			
Si	3s	−17.3	1.63			
	3p	−9.20	1.43			
Ti	4s	−8.97	1.50			
	4p	−5.44	1.50			
	3d	−10.81	4.55	1.60	0.4391	0.7397
Fe	4s	−9.22	1.90			
	4p	−5.37	1.90			
	3d	−12.28	5.55	1.80	0.5366	0.6678

[a] Contraction coefficients used in the double-ζ expansion.

The p_y bands are appropriately labeled as π levels in the molecular network as the interaction between dimers is reduced. Since the σ_p and σ_p* levels of graphite have π_y* and π_y character, respectively, they have different symmetry characteristics in D_{2h} and undergo an allowed crossing. However, the π_y* band and the σ_x* band have identical symmetry properties in the Brillouin zone except at Γ. Therefore, the bands may not cross at general points in the zone, yet their chracteristics swap at the zone center. This avoided crossing accounts for the fifth occupied level in the molecular structure. The σ_x* level at Γ contains a significant contribution from σ_{2s}* which reduces the interaction within the dimers, eq 2. In the isolated molecules they become the σ_{2s}* levels exclusively.

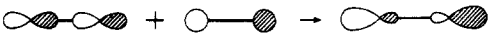

(2)

We point out that the analysis neglected the effects of any orbital interactions between the anionic network and the cations, which occupy sites coplanar with the dimers. Though the addition of these cation orbitals cannot change the symmetry arguments previously presented, they may relax the extent of the geometrical distortion of the network. Figure 13b does not predict insulating behavior for CaC_2 though the geometry of the carbon framework is nearly identical. Furthermore, these distorted graphite sheets are stacked relatively closely (CaC_2 is tetragonal). Questions regarding the energetic contributions of these additional structural considerations await further investigation.

Acknowledgment. This research was supported by the National Science Foundation via NSF DMR84141754 and DR8216892. We thank Prof. Ole Kleppa for several useful conversations and for making available his thermochemical data prior to publication.

Appendix

The geometries used for the various structures were as follows. For AlB_2 a "typical" geometry was used (see ref 6) with B–B distances of 1.75 Å and M–B distances of 2.338 Å. The interplanar separation was 3.1 Å. For the ReB_2 structure a B–B distance equal to that in the planar variant (AlB_2) was used, and the rest of the dimensions were those of the real ReB_2 structure[12] scaled accordingly. For the puckered AlB_2 arrangement, the sheets were separated an extra 0.1 Å over their separation in the planar analogue. For the fluorite and cadmium iodide structures an M–B distance of 2.35 Å was used. For the distortion of eq 1, leading to the CaC_2 structure, the dimensions of the hexagonal unit cell were kept fixed as above, and the inter- and intra-dimer distances varied by changing the value of x ($x \leq {}^1/_6$) in the atomic coordinates ($^1/_2$, $^1/_2$, $0 \pm x$, $-x$, 0). All the computations used the extended Hückel formalism to generate the energy bands with the parameters given in Table IV. A special k point set of 50 points within the irreducible wedge of the hexagonal Brillouin zone was used to generate the numerical results for these AlB_2 structures.

Registry No. ScB_2, 12007-34-0; TiB_2, 12045-63-5; VB_2, 12007-37-3; CrB_2, 12007-16-8; MnB_2, 12228-50-1; NiB_2, 12045-56-6; CoB_2, 11070-96-5; FeB_2, 12007-18-0; CaB_2, 103981-17-5.